(This is a sample cover image for this issue. The actual cover is not yet available at this time.)

Microstructural evolution of a Ni-based superalloy (617B) at 700 °C studied by electron microscopy and atom probe tomography

Darius Tytko [a],*, Pyuck-Pa Choi [a],*, Jutta Klöwer [b], Aleksander Kostka [a], Gerhard Inden [a], Dierk Raabe [a]

[a] *Max-Planck-Institut für Eisenforschung, Department for Microstructure Physics and Metal Forming, Max-Planck-Str. 1, 40237 Düsseldorf, Germany*
[b] *ThyssenKrupp VDM GmbH, Kleffstrasse 23, 58762 Altena, Germany*

Abstract

We report on the microstructural evolution of a polycrystalline Ni-based superalloy (Alloy 617B) for power plant applications at a service temperature of 700 °C. The formation of secondary $M_{23}C_6$-carbides close to grain boundaries (GBs) and around primary Ti(C,N) particles is observed upon annealing at 700 °C, where γ' is found to nucleate heterogeneously at $M_{23}C_6$ carbides. Using atom probe tomography, elemental partitioning to the phases and composition profiles across phase and grain boundaries are determined. Enrichments of B at $\gamma/M_{23}C_6$ and $\gamma'/M_{23}C_6$ interfaces as well as at grain boundaries are detected, while no B enrichment is found at γ/γ' interfaces. It is suggested that segregation of B in conjunction with γ' formation stabilizes a network of secondary $M_{23}C_6$ precipitates near GBs and thus increases the creep rupture life of Alloy 617B. Calculations of the equilibrium phase compositions by Thermo-Calc confirm the chemical compositions measured by atom probe tomography.
© 2011 Acta Materialia Inc. Published by Elsevier Ltd. All rights reserved.

Keywords: Atom probe tomography; Ni-based superalloy; Alloy 617B; $M_{23}C_6$; Boron enrichment

1. Introduction

The demand for energy is set to double over the coming decades [1]. In order to reduce CO_2 emissions from fossil power plants there is an urgent need to improve energy conversion efficiency [2]. To achieve this goal, the next generation of ultra-supercritical power plants must operate at service temperatures between 700 and 720 °C and steam pressures of up to 393 bar [3]. However, conventional ferritic steels (P92) used in current power plants cannot withstand such conditions [2,4], as they are designed for temperatures up to 600 °C and operating pressures up to 250 bar. Consequently, they are expected to be replaced by Ni-based superalloys which show longer creep rupture life and higher corrosion resistance [2,3].

One of the most promising superalloy candidates in this context is Alloy 617B (Ni–24.7Cr–11.4Co–5.2Mo–2.1Al–1Fe–0.02B, at.%) [3], which is a B-alloyed variant of the commercial Alloy 617. The properties of Alloy 617B include high creep rupture strength and good weldability [3], rendering it an excellent candidate material for membrane walls and superheater tubes in next-generation fossil-fuel power plants [3]. Since Alloy 617B is a newly developed material, only a few studies on the microstructure during operation have been done to date. Moreover, no reports exist on the role of B on the microstructural evolution of Alloy 617B. Wu et al. [5] studied the microstructure of long-term aged (approximately 65,000 h at a temperature range from 482 to 871 °C) Alloy 617 (Inconel 617) modified with 0.03 at.% B; their main findings were as follows. (1) The primary particles were Ti(C,N), γ', M_6C and $M_{23}C_6$. Except for Ti(C,N), all phases revealed coherent orientation relationships with the matrix. (2) The morphology of the $M_{23}C_6$ particles was found to be plate/rod-shaped. (3) $M_{23}C_6$ tended to cluster with

* Corresponding authors. Tel.: +49 211 6792 180; fax: +49 211 6792 333 (D. Tytko), tel.: +49 211 6792 167; fax: +49 211 6792 333 (P. Choi).
E-mail addresses: d.tytko@mpie.de (D. Tytko), p.choi@mpie.de (P.-P. Choi).
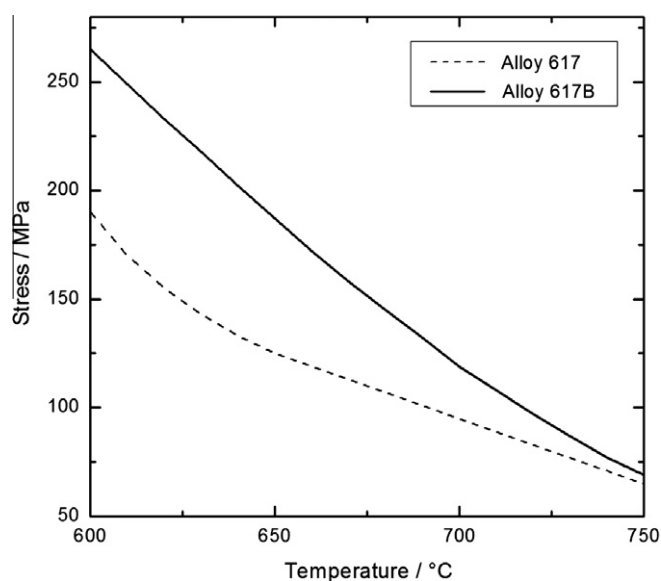
Fig. 1. Creep rupture strength of Alloy 617 (Nicrofer5520Co) and Alloy 617B (Nicrofer 5520 CoB) between 600 and 750 °C (10^5 h) [6].

increasing time and temperature. (4) The thermal stability of Inconel 617 was assessed by the authors to be good over a temperature range from 482 to 704 °C. Beyond this temperature range carbide decomposition, coarsening and agglomeration was observed.

Fig. 1 presents the creep rupture strength of Alloy 617B as compared to the conventional Alloy 617 [6]. Alloy 617B exhibits a 25% higher creep rupture strength (119 MPa after 100,000 h operation at 700 °C) than Alloy 617, indicating that an addition of B has a substantial beneficial influence on the creep behavior of this material. However, the underlying mechanisms for enhancing the creep properties of Alloy 617 by B additions have yet to be clarified. As a first step to address this issue, the microstructure and corresponding B distribution must be characterized at the service temperature (700 °C) for various annealing times. For this purpose, scanning electron microscopy (SEM) and transmission electron microscopy (TEM) studies were done in this work in conjunction with atom probe tomography (APT). The APT results on solute partitioning were compared with Thermo-Calc calculations, which are based on the minimization of the Gibbs free energy of the system.

2. Experimental

The as-received material was a sheet of Alloy 617B provided by ThyssenKrupp VDM (Nicrofer 5520 CoB™), which was produced by continuous casting of a 210 mm thick rectangular electrode, ESR-remelting (6.5 ton ingots),

hot-rolling of the remelted slab to 30 mm thick plates between 1000 and 1200 °C, and subsequent intermediate diffusion annealing at 1230 °C. The plates were homogenized at 1175 °C for 1 h and subsequently quenched in water. The nominal chemical composition of the as-received sample, as determined by wet chemical analysis, is shown in Table 1.

The samples were annealed at 700 °C for 10, 100 and 1000 h in air and quenched in water.

TEM samples were prepared by a standard electropolishing technique using a Struers Tenupol (double-jet) device. Discs 3 mm in diameter were cut out of the bulk material and mechanically polished to about 100 μm in thickness. Electropolishing was carried out at −30 °C at a voltage of 16 V, using a solution of 90% ethanol and 10% perchloric acid. TEM investigations were conducted on a JEOL JEM-2200FS operated at 200 kV.

SEM and energy dispersive X-ray spectroscopy (EDX) analyses were performed using a JEOL JSM-6500F microscope.

Polished samples were also used for site-specific preparation of APT samples from a grain boundary region using the lift-out method and a dual-beam focused-ion-beam (FEI Helios NanoLab 600). The sample preparation procedure is described elsewhere [7–9].

APT investigations were carried out using a local electrode atom probe (LEAP 3000X HR, Cameca Instr.) [10]. As the samples were prone to fracture due to the presence of carbides, they were analyzed in pulsed laser mode, applying laser pulse energies of 0.4 nJ. The specimen base temperature and pulse repetition rate were set to ∼60 K and 250 kHz, respectively.

Thermo-Calc (database TTNI8) and DICTRA (database MOBNI) were used for equilibrium phase calculations and kinetics, respectively. The software and corresponding databases were provided by Thermo-Calc Software AB, Stockholm, Sweden.

3. Results

3.1. SEM and TEM

SEM images of the as-received material reveal a polycrystalline microstructure (grain sizes ranging from 300 to 500 μm) and some annealing twins (Fig. 2a). The presence of block-shaped primary Ti(C,N)-particles was confirmed by combined SEM and EDX analyses. These particles are found to be preferentially located at the grain boundaries (GBs).

The SEM images in Fig. 2a and b also reveal serrated GBs, which are decorated with primary carbides. After

Table 1
Chemical composition of as-received Nicrofer 5520 CoB sheet determined by wet chemical analysis (at.%).

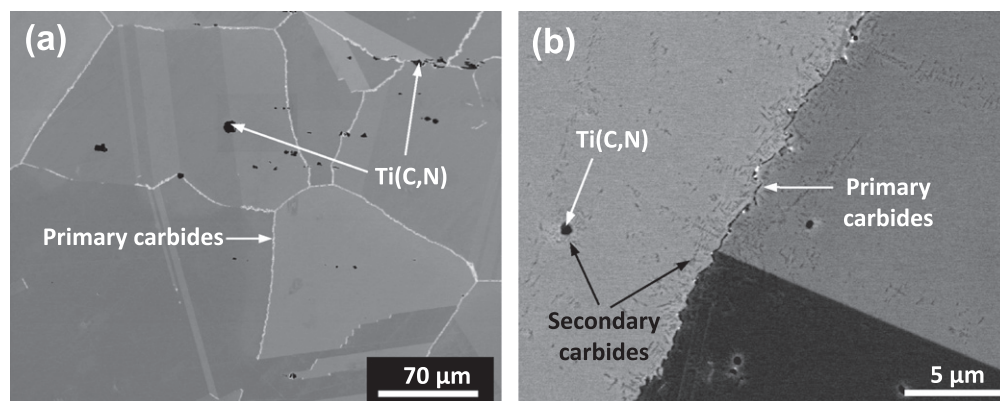| Ni	Cr	Co	Mo	Al	Fe	Ti	C	Si	N	Mn	Cu	B
Bal.	24.7	11.4	5.2	2.1	1.0	0.4	0.3	0.3	0.1	0.06	0.03	0.02

Fig. 2. SEM images of (a) the as-received state and (b) a sample annealed at 700 °C for 100 h. The latter image shows secondary carbide formation close to GBs and Ti(C,N) particles. Straight lines indicate twin boundaries.
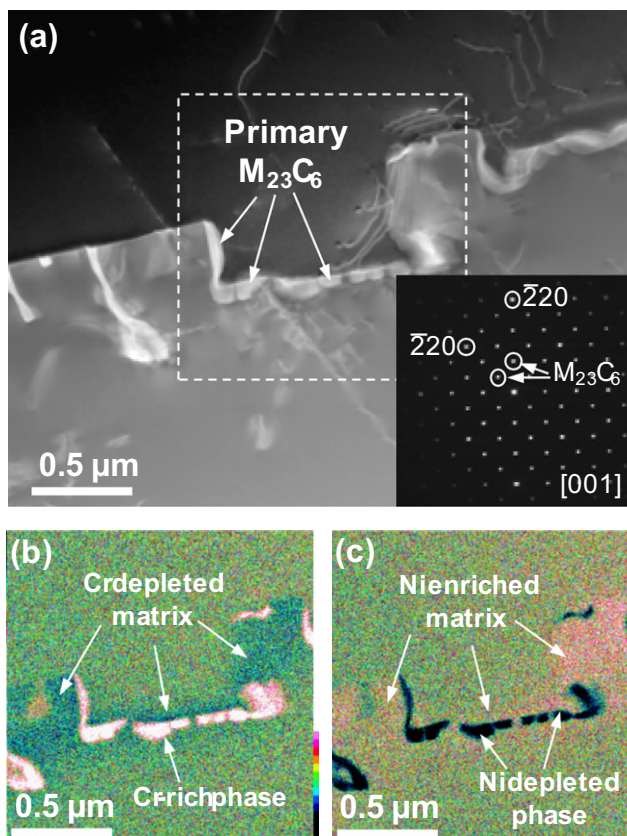

Fig. 3. (a) HAADF micrograph of a GB region of an as-received sample. $M_{23}C_6$ carbides decorate the GB. The selected-area diffraction (SAD) shows the coherency of both the $M_{23}C_6$ particles and the γ matrix. The circles in the SAD pattern mark the (-220) and (020) diffraction spots of the γ matrix and $M_{23}C_6$, respectively. (b,c) STEM–EDX maps of Cr and Ni taken from the dashed square in (a).

heat treatment at 700 °C for 100 h a network of fine secondary carbides formed close to the GBs and Ti(C,N)-particles (see Fig. 2b).

TEM analyses of the as-received sample revealed that grain boundaries are decorated by large primary $M_{23}C_6$ carbides (see Fig. 3). These observations are in agreement with previous studies on Inconel 617 by Jo et al. [11,12].

Selected-area diffraction (SAD) analysis (see inset in Fig. 3a) shows that the $M_{23}C_6$ particles are coherent with the γ matrix. The EDX maps presented in Fig. 3b and c show that regions close to the GB carbides are enriched with Cr and depleted in Ni. The surrounding matrix reveals complementary depletion or enrichment, respectively.

TEM images of the microstructure after annealing at 700 °C for 10 h are presented in Fig. 4a–c. Two additional phases appear as compared to the as-received material. (i) Close to the primary $M_{23}C_6$ carbides at the GBs, γ' ($L1_2$ ordered phase) precipitates have been formed in a high number density (marked by white arrows in Fig. 4a). (ii) A dense network of secondary $M_{23}C_6$ carbides has been formed inside the γ grains (Fig. 4a–c). The secondary carbides have a plate-shaped morphology and are up to 20 nm in thickness and 200 nm in length. Secondary $M_{23}C_6$ carbides strongly pin present dislocations within the microstructure (visible in bright contrast in Fig. 4a). All the observed phases are in coherence with each other as shown by SAD analyses (see inset in Fig. 4b).

Fig. 4c is a magnified image of the region in Fig. 4b marked by a white square. Using a high-angle annular dark field (HAADF) detector an image contrast is obtained, which is dependent on the atomic number, Z. The HAADF image in Fig. 4c reveals that secondary $M_{23}C_6$ carbides have heterogeneous chemical composition. Some of the particles, such as the one in the upper right corner of Fig. 4c, have uniform bright contrast, while the others have a dark core and a bright wavy envelope. Furthermore, dark regions at the interface between the carbide and matrix indicate the nucleation of ellipsoidal γ' particles with a major axis length of about 20 nm.

After annealing at 700 °C for 100 h a dense network of secondary carbides forms close to GB region, as seen in the HAADF images in Fig. 5a. At higher magnifications γ' particles, which have nucleated at the face sites of secondary $M_{23}C_6$ carbides, can clearly be resolved (Fig. 5b). As expected, γ' has undergone coarsening during prolonged annealing. The γ' particles exhibit an ellipsoidal shape, where the average length of the major axis is about
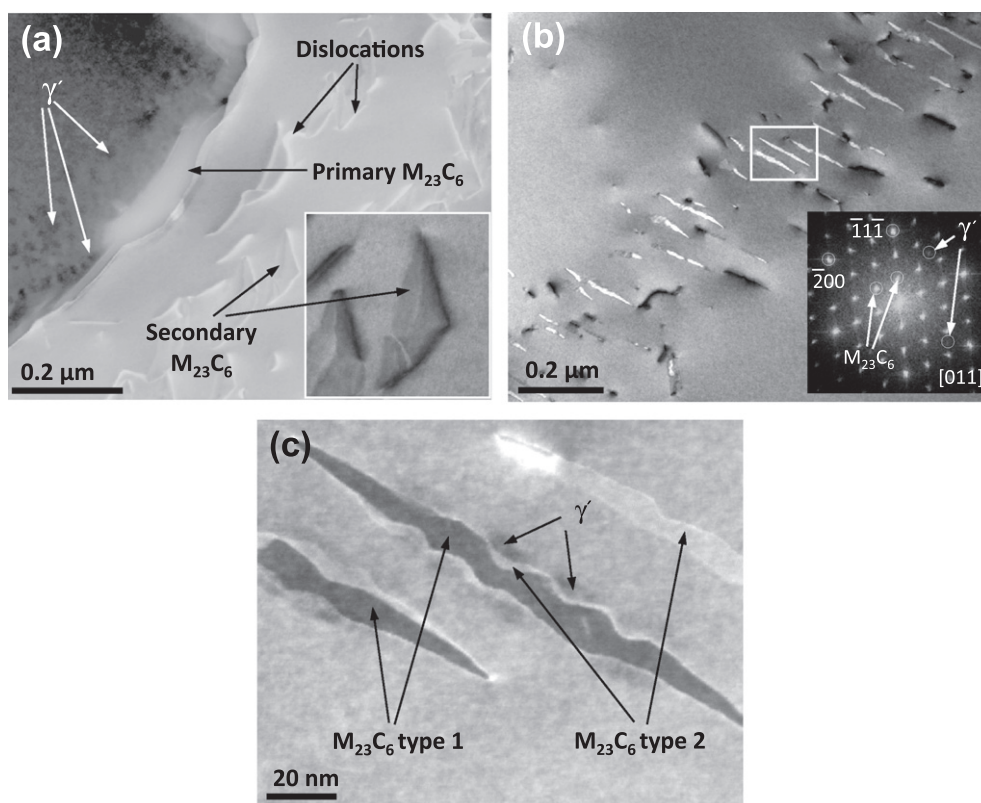
Fig. 4. STEM micrographs of the specimen annealed at 700 °C for 10 h. (a) Accumulation of γ' precipitates near primary GB carbide. (b) Network of coherent secondary $M_{23}C_6$ carbides and corresponding SAD. (c) STEM image using a HAADF detector, indicating compositional differences between secondary carbides.
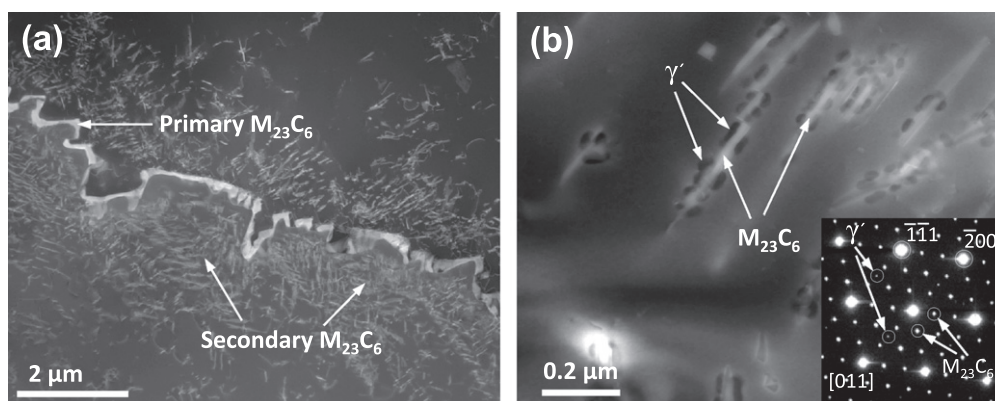

Fig. 5. (a) HAADF micrographs of the specimen annealed at 700 °C for 100 h. A dense network of secondary $M_{23}C_6$ carbides has been formed close to the primary $M_{23}C_6$ at the GB. (b) These elongated secondary $M_{23}C_6$ carbides are surrounded by γ' precipitates (arrows pointing down). The corresponding SAD pattern (inset in the micrograph) includes both phases present in the microstructure. $(-1 -1 1)$ and $(-2 0 0)$ diffraction spots marked by circles correspond to the γ matrix.

50 nm. SAD analyses (see inset in Fig. 5b) again reveal coherency between all phases present.

The sample aged at 700 °C for 1000 h (Fig. 6a) reveals significantly coarsened primary as well as secondary $M_{23}C_6$ particles. At this stage, the γ' particles at secondary $M_{23}C_6$ carbides exhibit a spherical shape with an average diameter of 70 nm. The fraction of $M_{23}C_6$ is found to increase in the grain interior with increasing annealing time, where γ' precipitates are also found at these inner grain carbides.

3.2. APT

Fig. 7a shows a TEM picture of an as-received tip sample prepared for APT analysis. After locating the GB in the sample, a final low kV FIB-polishing step was done. Fig. 7b and c present the elemental distribution map of this sample containing the GB and a concentration depth profile across the GB, respectively. Substantial enrichments of Cr, Mo, B and C are detected in the grain boundary region,
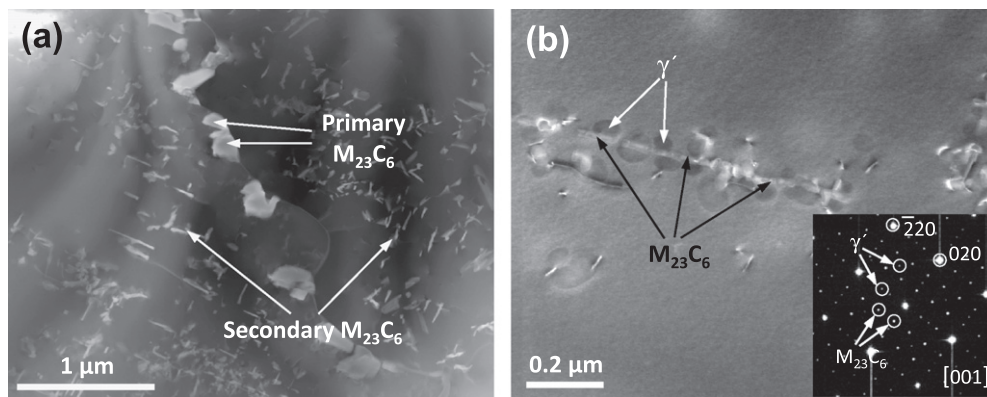
Fig. 6. (a) HAADF micrographs of the specimen annealed at 700 °C for 1000 h. Coarsened primary and secondary $M_{23}C_6$ carbides can be seen. (b) Spherical γ' precipitates (arrows pointing down) surrounding the secondary $M_{23}C_6$ carbides (arrows pointing up). The corresponding SAD pattern (included in the lower right part of the micrograph) relates to both phases present in the microstructure. Highlighted (-220) and (020) planes correspond to the matrix.
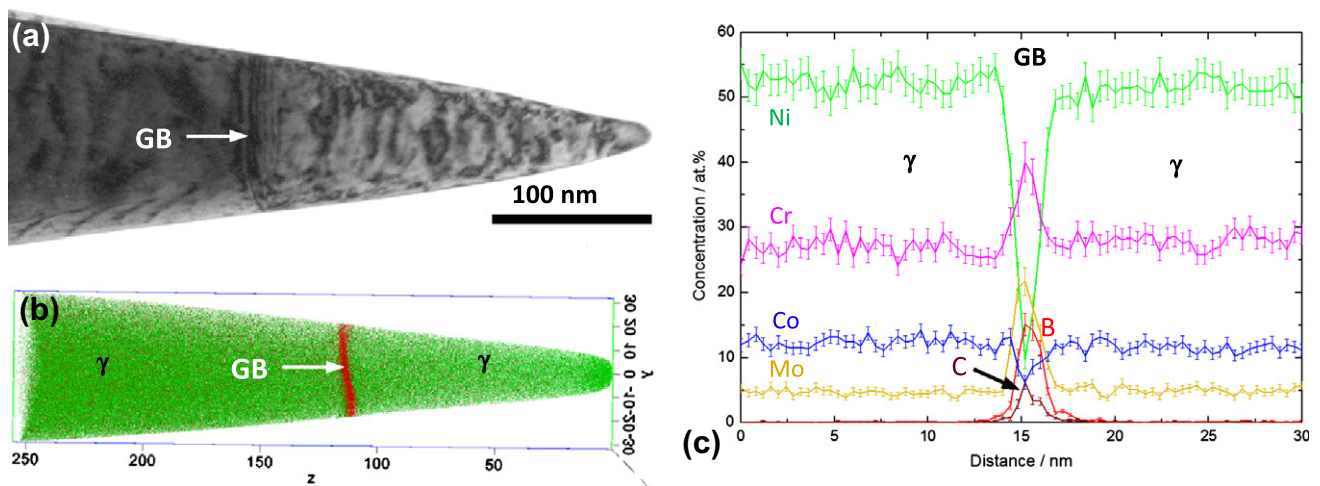

Fig. 7. (a) Tip imaged by TEM before final FIB polishing and APT measurement. The sample contains a GB (marked with a white arrow). (b) GB of the as-received material measured by means of atom probe. For clarity only Ni (green) and B (red) atoms are displayed. (c) Concentration profile along the white arrow in (b). Significant enrichments of Cr, Mo, B, and C at the GB are revealed.

whereas Co is slightly and Ni is strongly depleted. In order to confirm these findings a second APT measurement of a neighboring GB zone was performed, resulting in nearly identical segregation profile of the elements. As shown by TEM, primary $M_{23}C_6$ particles decorate the grain boundaries of Alloy 617B. These $M_{23}C_6$ particles could be detected by means of APT in as-received samples as well as annealed samples.

Composition profiles across secondary $M_{23}C_6/\gamma$ phase boundaries, plotted as proximity histograms [13,14], are shown in Fig. 8a–d, whereas Fig. 8f presents the concentration profile across a $M_{23}C_6/\gamma'$ interface. The error bars represent the 2σ deviation error. While all $M_{23}C_6/\gamma$ as well as $M_{23}C_6/\gamma'$ interfaces exhibit B enrichment, no B is detected at γ/γ' interfaces. The latter observation is in agreement with previous atom probe investigations on B-containing Ni-based superalloys [15,16]. Due to the nearly parallel ori-

entation of the detected $M_{23}C_6/\gamma$ interfaces and the local magnification effect [17], the B concentration peaks in Fig. 8b and d are smeared out.

Fig. 8e shows the elemental map of a sample annealed at 700 °C for 100 h. It can be seen that the APT results are in excellent agreement with TEM observations, showing γ' precipitates adjacent to $M_{23}C_6$ carbides. While B is preferentially located at the $M_{23}C_6/\gamma$ and $M_{23}C_6/\gamma'$ interfaces, no B is detected at γ/γ' interfaces. The measured phase compositions are listed in Table 2.

As expected, Al and Ti are strongly enriched in the γ' phase, whereas Cr, Co and Mo are depleted. The $M_{23}C_6$ carbide mainly consists of Cr ($\sim$66 at.%) and smaller amounts of Mo ($\sim$9.5 at.%), Ni ($\sim$4.1 at.%) and Co ($\sim$2.5 at.%), while no Al and Ti are detected in the carbide. The stoichiometry of this carbide phase corresponds to $M_{23}C_6$. The TEM-EDX maps shown in Fig. 3a–c indicate
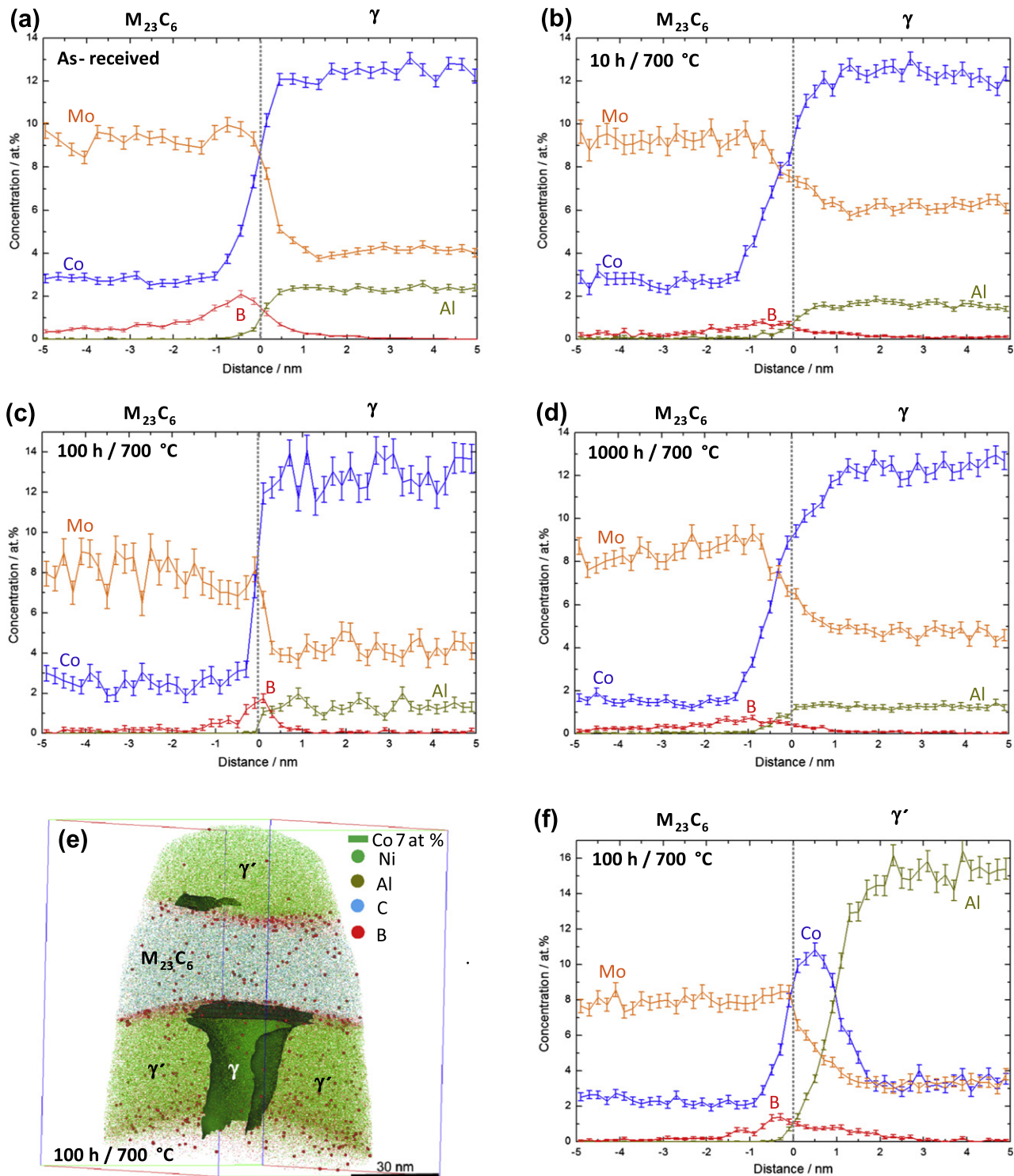
Fig. 8. APT data and concentration profiles across $M_{23}C_6/\gamma$ interfaces; (a)–(d) show concentration profiles across $M_{23}C_6/\gamma$ interfaces for the as-received state as well as samples annealed at 700 °C for 10, 100 and 1000 h, respectively. B enrichments at the $M_{23}C_6/\gamma$ phase boundaries are detected. (e) Elemental distribution map of the sample annealed at 700 °C for 100 h. In agreement with TEM observations, a γ' precipitate adjacent to a $M_{23}C_6$ particle is displayed. The γ phase is visualized by an isoconcentration surface of 7 at.% Co. Enrichments of B at the $M_{23}C_6/\gamma'$ interfaces can be observed as well. (f) Corresponding to the measurement in (e) a concentration profile across the $M_{23}C_6/\gamma'$ interface is shown. B enrichment as well as pile-up of Co at the $M_{23}C_6/\gamma'$ interface is found. The error bars in the profiles correspond to 2σ deviation errors.

an enrichment of Ni as well as depletion of Cr around the $M_{23}C_6$ particle. Due to the weak Al signal, an Al-rich zone around the carbide could not be detected by EDX, but was

proven via compositional atom probe analysis of a matrix region close to a $M_{23}C_6$ particle (see Table 3). The matrix region surrounding $M_{23}C_6$ particles contains 40% more

Table 2
Chemical composition as measured by APT. Phase compositions (at.%) were determined for a sample annealed at 700 °C for 100 h.

	Ni	Cr	Co	Mo	Al	Fe	Ti	C	B
γ	59.8 ± 0.12	18.8 ± 0.06	13.0 ± 0.08	4.3 ± 0.05	2.2 ± 0.03	1.2 ± 0.02	0.3 ± 0.02	0.05 ± 0.01	0.0
γ'	72.0 ± 0.05	2.6 ± 0.02	3.8 ± 0.02	2.7 ± 0.01	14.9 ± 0.03	0.4 ± 0.01	3.0 ± 0.02	0.06 ± 0.01	0.0
$M_{23}C_6$	4.1 ± 0.02	65.5 ± 0.03	2.5 ± 0.01	8.4 ± 0.02	0.0	0.6 ± 0.01	0.0	18.8 ± 0.1	0.03 ± 0.002

Table 3
Local composition variation (at.%) in the matrix in grain interior and close to $M_{23}C_6$ as measured with APT (as-received sample).

	Ni	Cr	Co	Mo	Al	Ti
γ (grain interior)	53.5 ± 0.015	25.1 ± 0.01	11.6 ± 0.006	5.9 ± 0.006	2.0 ± 0.002	0.35 ± 0.002
γ (close to $M_{23}C_6$)	59.7 ± 0.138	18.4 ± 0.173	13.5 ± 0.129	3.6 ± 0.085	2.8 ± 0.42	0.45 ± 0.031

Table 4
Composition (at.%) of the main elements of Alloy 617B used for thermodynamic calculations.

Ni	Cr	Co	Mo	Al	Fe	Ti	Si	N	C	B
Bal.	24.7	11.4	5.2	2.1	1.0	0.4	0.3	0.1	0.3	0.02

Al, 28% more Ti, 12% more Ni, 27% less Cr and 39% less Mo relative to the matrix in the grain interior.

Previous studies on the site preferences of solute elements in γ' (Ni$_3$Al) revealed that Cr, Mo, Fe and Ti preferentially occupy Al sites in γ' [18–22], whereas Co shows a strong tendency to substitute Ni [23]. Taking into account these site preferences, the measured APT compositions yield the stoichiometry of γ'.

3.3. Thermo-Calc

In order to validate the APT data, thermodynamic calculations were performed using the software Thermo-Calc, which is based on the Calphad method [24]. The TTNI-8 database for Ni-based superalloys was used for the calculations. The nominal composition was used for the calculations (Table 4). For 700 °C, γ, γ', Ti(C,N), Mu-phase, $M_{23}C_6$ and M_3B_2 are predicted as equilibrium phases by Thermo-Calc. When eliminating the phases, which are not experimentally observed, more accurate thermodynamic predictions can be obtained as demonstrated by Miller et al. [25]. Thus, in the present case only γ, γ', Ti(C,N) and $M_{23}C_6$ were considered for further calculations. In Table 5 the calculated equilibrium compositions of γ, γ', Ti(C,N) and $M_{23}C_6$ at 700 °C are listed. It should be noted that Thermo-Calc predicts the existence of two different $M_{23}C_6$ carbides with strongly differing B content (see Table 5).

4. Discussion

4.1. GB chemistry

As observed by SEM and TEM, the as-received sample exhibits primary $M_{23}C_6$ carbides which decorate the grain boundaries. These particles are typically about 0.2 μm in thickness (compare Fig. 3). However, the GBs are not homogeneously decorated by carbides. Fig. 7 shows a GB region where only a thin carbide film is precipitated. Here, a strong variation in composition is observed within a range of about 3 nm. The Ni content is drastically reduced, while Co is slightly depleted and Cr, Mo, B and C are significantly enriched (Fig. 7c). Under the assumption that B substitutes C the local composition in this thin plate-like precipitate corresponds to the stoichiometry of $M_{23}(B,C)_6$. The high B content of $M_{23}(B,C)_6$ is most likely the result of cooling. According to the mobility database MOBNI, the mobility of B in the γ matrix is much higher than that of C. Consequently, at the very early stages of $M_{23}C_6$ formation the flux of B from γ towards the growing $M_{23}C_6$ particle is higher than that of C, leading to a high B concentration in $M_{23}C_6$. Furthermore, at lower temperatures ($T \leqslant 800$ °C) a B-rich modification of $M_{23}(B,C)_6$ becomes stable (denoted $M_{23}C_6$#2 in Table 5). Simulations performed with DICTRA showed that the formation of a thin B-rich $M_{23}(B,C)_6$ precipitate is completed within seconds after nucleation. These results show that $M_{23}(B,C)_6$ can form even at very high cooling rates, and definitely will form under technical production conditions.

4.2. Formation of precipitates

Primary $M_{23}C_6$ carbides located at the GB were observed in the as-received state (Fig. 3a) as well as in heat-treated samples (Figs. 4a, 5a, 6a). Moreover, secondary $M_{23}C_6$ were found close to GBs and Ti(C,N) particles in annealed samples (Figs. 2b and 5a). Secondary carbides, together with the γ' phase, are reported to form as products of the decomposition of primary MC-carbides upon annealing [26,27]. In the present study, secondary $M_{23}C_6$ were observed to form around Ti(C,N)-particles (see Fig. 2b), where Ti(C,N) provides C for secondary carbide

Table 5
Calculated equilibrium compositions (at.%) of a sample annealed at 700 °C for 100 h. Borides were excluded from the Thermo-Calc equilibrium calculations.

	Ni	Cr	Co	Mo	Al	Fe	Ti	Si	N	C	B
γ	55.0	24.6	11.7	5.2	1.9	1.0	0.13	0.3	$1.7 \cdot 10^{-6}$	$6 \cdot 10^{-4}$	$3.1 \cdot 10^{-3}$
γ'	71.3	2.5	3.3	0.7	13.4	0.13	8.2	0.37	0.0	0.0	0.0
$M_{23}C_6$ #1	5.3	61.8	2.0	10.2	0.0	0.09	$4 \cdot 10^{-6}$	0.0	0.0	20.5	0.23
$M_{23}C_6$ #2	2.4	74.0	2.0	0.7	0.0	0.17	$4 \cdot 10^{-7}$	0.0	0.0	12.7	8.0
Ti(C,N)	50.0	$1.2 \cdot 10^{-3}$	0.0	0.0	0.0	0.0	0.0	0.0	49.38	0.6	$7.1 \cdot 10^{-4}$

formation. In addition, dislocations close to GBs and the incoherent Ti(C,N)-precipitates may contribute to the formation of secondary carbides, since $M_{23}C_6$ is reported to show a strong tendency to nucleate at lattice defects such as dislocations or GBs [28,29]. Hence, the described circumstances give beneficial conditions for carbide nucleation. Promoting the formation of Ti(C,N) in this material aims at controlling the grain size [30]. However, the downside of this mechanism is that these particles are incoherent with the matrix and thus give rise to a high dislocation density. The latter effect can increase the creep rate, as accumulated dislocations can act as sources for dislocation multiplication and lead to stress concentrations and microcracks.

The secondary carbides are concentrated in a range of about 2 μm close to the GB. This is obviously due to the fact that the GB acts as a source of vacancies. The composition of $M_{23}C_6$ is very different from the γ matrix. Thus, the formation and growth of $M_{23}C_6$ particles requires transport of a considerable amount of all elements. Secondary $M_{23}C_6$ carbides were found to have two different chemical compositions after annealing at 700 °C for 10 h as revealed by different atomic Z contrast in Fig. 4c. Such an observation is in good agreement with previous reports by other authors, where a variant of $M_{23}C_6$ with a higher B content was found [35–37]. Since the investigated Alloy 617B is enriched with B, the findings are not unusual. Moreover, equilibrium calculations using Thermo-Calc also predict two types of $M_{23}C_6$ for this material (see Table 5). A significant variation of Cr and Mo content in the two types of $M_{23}C_6$ is determined, which should lead to the observed HAADF contrast (Fig. 4c). The reliability of the thermodynamic data is discussed in Section 4.3.

Upon formation of $M_{23}C_6$, the surrounding γ matrix around the carbide particle has a composition strongly differing from the bulk composition (see e.g. Fig. 3b and c). Both APT analyses and ThermoCalc predictions (Tables 2 and 5, respectively) reveal that $M_{23}C_6$ contains no Al and Ti and only small amounts of Ni. As a consequence, the matrix region surrounding the carbide is rich in the rejected γ'-forming elements, while Cr as a $M_{23}C_6$-forming element is depleted in this region (see Table 3). Thus, the driving force for the nucleation of γ' at the existing $M_{23}C_6/\gamma$ interface is expected to be strongly enhanced as suggested by Yan et al. [31]. Hence, a correlated growth of $M_{23}C_6$ and γ' is observed, which leads to a heterogeneous distribution of γ'. Moreover, we observe that the

width of the depletion zone of Al and Ti depends on the size of the $M_{23}C_6$ particle and that the number density of γ' particles nucleated at the coarse primary $M_{23}C_6$ particles is larger compared to the smaller secondary $M_{23}C_6$ particles (see Fig. 4a and c).

In general, it was observed that $M_{23}C_6$ particles grow in the elastically soft (1 0 0)-directions of the matrix, resulting in plate-shaped particles with an aspect ratio of up to 10:1. The formation of γ' envelopes is expected to inhibit the growth of $M_{23}C_6$ by constraining the diffusion of Cr and Mo. The TEM image in Fig. 4c supports this argument. It can clearly be seen that γ' prevent coarsening of secondary $M_{23}C_6$ carbides, giving rise to a wavy shape of the particles.

4.3. Evaluation of thermodynamic data

The comparison between Thermo-Calc results and the experimentally determined compositions of γ, γ' and $M_{23}C_6$ after 100 h annealing yields good agreement. However, one has to take into account the experimentally observed local compositional variations when evaluating Thermo-Calc data. In fact, it could be shown that the matrix compositions in the bulk and close to the matrix/carbide interface differ strongly due to rejection and enrichment of certain elements during growth of the carbides (see Table 3). As a consequence, the global composition of the γ–phase (calculated by Thermo-Calc) shows a relative deviation from the local composition (measured by APT) by 10 at.% and 33 at.% for Ni and Cr, respectively. In addition, minor deviations between the measured and calculated compositions can arise from measurement errors associated with the APT method. These can be caused by preferential field-evaporation of certain elements and by statistical uncertainties [32,33]. On the other hand, the calculated compositions can be inaccurate due to an incomplete database or due to the fact that the system is still in a transient state. In summary, there are several aspects to consider when comparing experimental and computational data.

4.4. Interface analysis

Previous studies on carbide precipitation in stainless steels by means of atom probe field ion microscopy (APFIM) revealed enrichments of B inside $M_{23}C_6$ [33–35]. Lundin and Richarz investigated B-doped Cr-rich

steels for power plant applications by APFIM [34]. The authors found B-enriched $M_{23}C_6$-carbides and P segregation at the $M_{23}C_6/\gamma$ interface after long-term aging at 480 °C. Within the detection limit of the one-dimensional atom probe used in their study, no B segregation could be detected in their work.

As shown in Fig. 8a–d, we were able to observe B enrichment at the $M_{23}C_6/\gamma$ interface in the as-received as well as annealed states of Alloy 617B. Moreover, an enrichment of B at the $M_{23}C_6/\gamma'$ interface was detected in the sample annealed for 100 h (see Fig. 8f). To quantify the enrichments, the Gibbs interfacial excess was determined by integrating the B-enriched area of the concentration profiles according to the procedure described in Refs. [35,36]. Based on our experimental results, the interfacial excess of B at $M_{23}C_6/\gamma$ is nearly equal in all heat-treated states, with an average value of $2.55 \pm 0.34 \times 10^{14}$ atoms cm^{-2}.

In the case of the $M_{23}C_6/\gamma$ interface, the B enrichment may be related to the kinetics. At first, in the nucleation stage the boundary condition at the moving $M_{23}C_6$ interface leads to a slightly increased B content due to the faster diffusivity of B compared to C. During $M_{23}C_6$ growth, the B content takes the equilibrium value of about 0.2 at.%. Consequently, there is no B enrichment at the moving boundary during growth. The observed B enrichment at this boundary is then the result of the cooling process. During cooling, B diffusion is dominant relative to C. This leads again to the observed B enrichment on the nanometer scale. These conclusions are based on first results obtained from simulations with DICTRA in conjunction with the mobility database MOBNI.

Besides revealing the B distribution, Fig. 8f also shows an enrichment of Co between $M_{23}C_6$ and γ'. This enrichment can essentially be explained by the fact that Co has a low solubility in both $M_{23}C_6$ and γ' (see Tables 2 and 5). While $M_{23}C_6$ and γ' coarsen, the Co is rejected, leading to a pile-up between the two phases boundary on the heterointerface.

4.5. Secondary carbide network

The growth of $M_{23}C_6$ particles is expected to be inhibited by the formation of γ' envelopes. These layers suppress the diffusion of $M_{23}C_6$-forming elements. Furthermore, B segregation to the $M_{23}C_6/\gamma$ is expected to lower the interfacial energy and mobility, also contributing to an inhibited growth of $M_{23}C_6$ particles. As a consequence a stable network of secondary $M_{23}C_6$ particles is formed. On the one hand, such highly dispersed network of fine secondary carbides is able to retard the spread of dislocations during creep, where the obstacles delay the accumulation of dislocations at GBs and postpone the formation of microcracks. On the other hand, the decelerated carbide coarsening prolongs the expansion of the carbide film at the GBs, which is known to deteriorate the mechanical properties of the material [37]. These considerations suggest that Alloy 617B may have a more stable microstructure than its B-depleted counterpart Alloy 617, which explains the observed enhancement in the creep rupture strength of Alloy 617B as shown in Fig. 1. More detailed comparative studies of the microstructure of these two alloys are currently being undertaken.

5. Conclusions

A polycrystalline Ni-based superalloy (Alloy 617B) was studied with respect to its microstructural evolution at a service temperature of 700 °C using a combination of SEM, TEM and APT. The grain boundaries in this alloy were of serrated shape and decorated with $M_{23}C_6$ particles. In addition, a phase with a composition close to $M_{23}C_6$, though with a higher B content, was detected. After thermal exposure at 700 °C formation of secondary $M_{23}C_6$ carbides coherent with the γ matrix and heterogeneous nucleation of γ' particles at $M_{23}C_6/\gamma$ interfaces were observed. The latter is due to an enrichment zone of γ'-forming elements around $M_{23}C_6$. APT provided chemical composition maps of γ, γ' and $M_{23}C_6$ in good agreement with Thermo-Calc results. Deviations between experiment and simulation mainly arise from the local compositional variations of the matrix close to the $M_{23}C_6/\gamma$ interfaces. Furthermore, B enrichments at the $M_{23}C_6/\gamma$ and $M_{23}C_6/\gamma'$ phase boundaries were detected, which can be explained by diffusive competition between C and B in the early nucleation stage and during quenching. On the other hand, no B enrichment at the γ/γ' interface was detected.

Interfacial B enrichments and γ' formation at $M_{23}C_6$ are believed to slow down the growth of $M_{23}C_6$ particles and thus preserve a stable precipitation network of coherent particles, increasing the creep resistance of this material. To support this assumption, comparative studies of the microstructural evolution of creep-deformed Alloy 617 and Alloy 617B samples are planned as future work.

References

[1] Klöwer J, Gehrmann B. ThyssenKrupp VDM GmbH special reprint SR1/08 2007:2.
[2] Bugge J, Kjær S, Blum R. Energy 2006;31:1437.
[3] Viswanathan R, Gandy D, Coleman K. Proc of the 5th EPRI. ASM International; 2008.
[4] Ennis PJ, Czyrska-Filemonowicz A. Sadhana 2003;28:709.
[5] Wu Q, Song H, Swindeman RW, Shingledecker JP, Vasudevan VK. Metall Mater Trans A 2008;39:2569.
[6] TÜV Rheinland report for babcock-Hitachi Europe GmbH, 926/W 031029; 2003.
[7] Thompson K, Lawrence D, Larson D, Olson J, Kelly T, Gorman B. Ultramicroscopy 2007;107:131.

[8] Miller MK, Russell KF, Thompson K, Alvis R, Larson DJ. Microscopy Microanal 2007;13:428.
[9] Felfer P, Ringer S, Cairney J. Ultramicroscopy 2011;111:435.
[10] Kelly TF, Miller MK. Rev Sci Instrum 2007;78:031101.
[11] Jo TS, Kim GS, Seo YI, Ryu WS, Kim YD. Mater Sci Forum 2007;544:411.
[12] Jo TS, Lim JH, Kim YD. J Nucl Mater 2010;406:360.
[13] Hellman OC, Vandenbroucke JA, Rüsing J, Isheim D, Seidman DN. Microscopy Microanal 2000;6:437.
[14] Miller M, Forbes R. Mat Char 2009;60:461.
[15] Sijbrandij SJ, Miller MK, Horton JA, Cao WD. Mater Sci Eng A 1998;250:115.
[16] Blavette D, Duval P, Letellier L, Guttmann M. Acta Mater 1996;44:4995.
[17] Vurpillot F, Bostel A, Blavette D. App Phys Lett 2000;76:3127.
[18] Almazouzi A, Numakura H, Koiwa M, Hono K, Sakurai T. Intermetallics 1997;5:37.
[19] Jiang C, Gleeson B. Scripta Mater 2006;55:433.
[20] Booth-Morrison C, Mao Z, Noebe RD, Seidman DN. App Phys Lett 2008;93:033103.

[21] Geng C, Wang C, Yu T. Acta Mater 2004;52:5427.
[22] Mekhrabov A, Akdeniz M, Arer M. Acta Mater 1997;45:1077.
[23] Sluiter MHF, Kawazoe Y. Phys Rev B 1995;51:4062.
[24] Spencer P. Calphad 2008;32:1.
[25] Miller MK, Babu SS, Burke MG. Mater Sci Eng A 2002;327:84.
[26] Lvov G, Levit VI, Kaufman MJ. Metall Mater Trans A 2004;35:1669.
[27] Qin X, Guo JT, Yuan C, Hou J, Ye HQ. Mater Sci Forum 2007;546:1301.
[28] Liu LR, Jin T, Zhao NR, Sun XF, Guan HR, Hu ZQ. Mater Sci Eng A 2003;361:191.
[29] Beckitt F, Clark B. Acta Metall 1967;15:113.
[30] Xu S, Dickson JI, Koul AK. Metall Mater Trans A 1998;29:2687.
[31] Yan B, Zhang J, Lou L. Mater Sci Eng A 2008;474:39.
[32] Seidman DN, Stiller K. MRS Bull 2009;34:717.
[33] Miller MK. J Vac Sci Technol 1981;19:57.
[34] Lundin L, Richarz B. App Surf Sci 1995;87:194.
[35] Krakauer BW, Seidman DN. Phys Rev B 1993;48:6724.
[36] Hellman OC, Seidman DN. Mater Sci Eng A 2002;327:24.
[37] Davis JR, Committee AIH. Nickel, cobalt, and their alloys. ASM International; 2000.